journal

J. Am. Ceram. Soc., **84** [6] 1361–68 (2001)

Structure and Chemistry of Yttria-Stabilized Cubic-Zirconia Symmetric Tilt Grain Boundaries

Elizabeth C. Dickey*,† and Xudong Fan‡

Department of Chemical and Materials Engineering, University of Kentucky, Lexington, Kentucky 40506-0046

Stephen J. Pennycook

Solid State Division, Oak Ridge National Laboratory, Oak Ridge, Tennessee 37831-6030

The atomic structures of two symmetric [001] tilt grain boundaries in yttria-stabilized cubic-zirconia, Σ5 (310) and near-Σ13 (510), are studied by *Z*-contrast scanning transmission electron microscopy. Both boundaries are composed of periodic arrays of highly symmetric structural units, with a distinct unit for each boundary. Oxygen *K*-edge electron energy-loss spectra show that the oxygen coordination is similar between the bulk and grain boundary, indicating that oxygen ions within the grain boundary reside in distorted tetrahedral sites. Atomic models of the grain boundaries are proposed that are consistent with the experimental data. The core structures are different from previously studied metal or oxide grain boundaries and are unique to the fluorite structure. Yttrium segregation to the grain boundaries is also investigated by electron energy-loss spectroscopy. Yttrium is found to segregate preferentially to the Σ5 grain boundary, and the spatial distribution of the segregation layer is confined to within 1 nm of the boundary plane.

I. Introduction

Pure tilt grain boundaries have been the subject of much research over the past 20 years, because they provide the opportunity for lattice imaging by transmission electron microscopy (TEM), and they have relatively small unit cells, which are conducive to atomic-scale modeling. Although general geometric[1,2] and bicrystallographic[3] models apply to all crystal classes, the specific core structures of the grain boundaries are dependent on the particular crystal structure and nature of bonding in the crystal. For example, the Σ5 (310) symmetric tilt boundary has been investigated in a number of metallic materials (e.g., copper,[4] niobium,[5] molybdenum,[6] and NiAl[7,8]) and, to a lesser extent, in oxide systems (e.g., NiO[9] and $SrTiO_3$[10,11]). Whereas the macroscopic degrees of freedom are identical for all the Σ5 (310) grain boundaries, significant differences are observed in the microscopic geometric degrees of freedom (i.e., rigid body translations) and the local atomic relaxations within the grain-boundary cores. Even between seemingly very similar materials, such as niobium and molybdenum (both body-centered cubic (bcc) metals), molybdenum has a rigid body translation of $a/2$ [001] along the tilt axis,[6] whereas niobium maintains mirror symmetry across the grain-boundary plane.[5] A general understanding of grain-boundary relaxation mechanisms remains to be realized and awaits more systematic experimental and theoretical investigations.

In this article, we investigate two [001] symmetric tilt grain boundaries in yttria-stabilized cubic-zirconia (YSZ). The grain boundaries in YSZ have important ramifications for the macroscopic mechanical and electrical properties of the material.[12–14] For example, it is observed that the grain-boundary resistivity is at least 1 order of magnitude larger than the bulk resisitivity.[15] The blocking effects of grain boundaries in calcia-doped zirconia have been observed even in relatively pure samples in which glassy or other grain-boundary phases are not present.[14] Although several studies have been conducted to understand the atomic structure and chemistry of YSZ grain boundaries,[14,16,17] none have reported the grain-boundary core structures (i.e., atomic positions). Here, we provide a detailed experimental analysis of two high-symmetry YSZ grain boundaries, the Σ5 (310)/[001] and the near-Σ13 (510)/[001] symmetric tilt boundaries. The grain boundaries are studied by *Z*-contrast scanning transmission electron microscopy (STEM), which reveals the projected cation sublattices parallel to the tilt axis. Electron energy-loss spectroscopy (EELS) is utilized to assess oxygen coordination in the grain-boundary core and to measure solute (Y^{3+}) segregation or depletion in the near-boundary region. Based on the experimental data, atomic models of the grain boundaries are developed. Although the tilt angles between the two boundaries (36.8° and 24°) vary by only 12.8°, two distinct grain-boundary core structures are observed. Furthermore, the solute segregation behaviors of the grain boundaries are very different, with preferential segregation to the 36.8°, Σ5, boundary. The two YSZ grain-boundary core structures are discussed in relation to each other and to other oxide grain-boundary structures derived in previous studies. The YSZ grain-boundary structures are the first developed for ionic crystals having the fluorite structure and contribute to our understanding of relaxation mechanisms in oxide grain boundaries. Moreover, they provide us with experimentally based atomic-scale models for future theoretical investigations.

II. Experimental Procedure

The YSZ bicrystals were stabilized in the cubic form with ~10 mol% Y_2O_3 (Shinkosha Co., Ltd., Yokohama, Japan). The first was a 36.8° symmetric tilt, [001] or Σ5 (310), bicrystal, and the second was a 24° symmetric tilt, [001], bicrystal only 1.4° from a perfect Σ13 (510) orientation. The tilt angles were confirmed by electron diffraction (see Fig. 1) as discussed below.

TEM samples were prepared from the bulk bicrystals along the [001] tilt axes by standard preparation techniques. A 2 mm × 1 mm rectangular plate containing the grain boundary was cut by a diamond wheel from the bulk specimen. The plates were mechanically polished to ~30 μm in thickness and then dimpled to ~15 μm. Finally, the specimens were thinned to electron transparency

T. E. Mitchell—contributing editor

Manuscript No. 188674. Received March 21, 2000; approved January 27, 2001.
Supported by the National Science Foundation, Division of Materials Research, under Grant No. DMR-9976851.

*Member, American Ceramic Society.
†Present address: Department of Materials Science and Engineering, The Pennsylvania State University, University Park, PA.
‡Also with the Solid State Division, Oak Ridge National Laboratory.

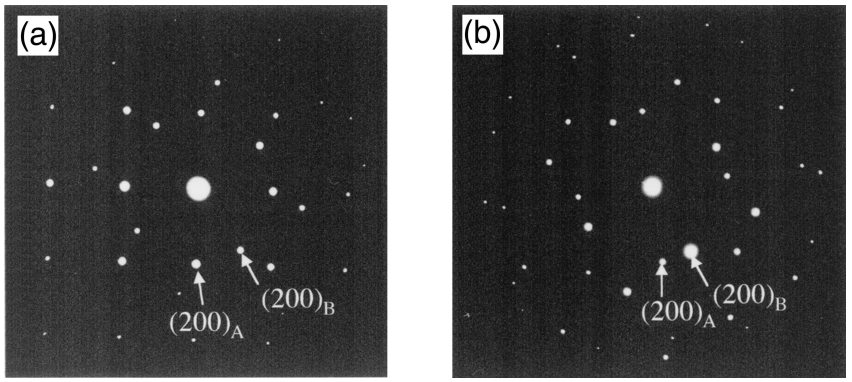

Fig. 1. Selected-area electron diffraction patterns of the (a) 36.8° and (b) 24° symmetric tilt [001] YSZ grain boundaries taken near the [001] zone axis.

by ion milling with 3 kV argon ions while cooled with liquid nitrogen.

The *Z*-contrast imaging was conducted at Oak Ridge National Laboratory using a dedicated STEM (Model HB603U, VG Microscopes, West Sussex, U.K.) operating at 300 kV and equipped with a high-resolution objective lens capable of forming a probe 0.13 nm in diameter. Incoherent images were formed with a high-angle annular dark-field detector having an inner detector angle of 50 mrad (~2.8°). With this large scattering angle, the intensities directly correspond to the projected potential distribution convoluted with the electron probe function.[18–20] Furthermore, because the scattering cross section of electrons used to form *Z*-contrast images scales with approximately the square of the atomic number, the projected cation column positions were revealed although almost no information regarding the oxygen positions was observed. Using a Lorentzian profile for the probe function, the object function, corresponding to cation column positions, was reconstructed by maximum-entropy image analysis.[21–24] The resulting object function, which represented the best fit to the experimental data, was used for quantitative analysis. All object functions presented below were convoluted with a Gaussian for better visibility. To assess the positional accuracy of the columns, images of the perfect crystal, far from any defect, were analyzed. The object function positions were compared with the known atomic column positions based on the crystal structure and a standard deviation of 0.2 nm calculated.

McGibbon *et al.*[24] give a thorough review of the factors that affect the accuracy of reconstructed *Z*-contrast images. Of particular interest to the present study is the effect of image visibility, defined as the image contrast divided by the square root of the background intensity, on positional deviations. The simulations performed by McGibbon *et al.* show that, even over a broad range of visibility, the positional deviations are not strongly affected, indicating that maximum entropy is a robust technique for noisy data.[24] Consequently, even though the total signal is typically reduced at grain boundaries because of strain-induced dechanneling, the positional accuracies in the maximum entropy-defined object function are similar to that in the bulk. The final step of the image analysis involves identifying similar structural units along the grain boundaries by computing cross correlation coefficients between various grain-boundary regions (similar to Ref. 25). Boundary units with high correlation are used to compute average grain-boundary structures with higher statistical accuracy.

EELS was conducted using a dedicated STEM (Model HB501UX, VG Microscopes) operating at 100 kV with an optimal probe diameter of 0.22 nm. The energy-loss spectrometer/detector system was originally supplied by the manufacturer and modified by McMullan.[26] Two quadrupoles were added at the exit slit of the spectrometer to magnify and project the energy-dispersive plane onto a yttrium aluminum garnet (YAG) scintillator. The image formed on the scintillator was optically coupled to an efficient air-cooled multiphase pinned charge-coupled device (CCD). The final spectrum was integrated into a maximum of 385 channels. This system provided high efficiency for the low signal levels encountered in the high energy-loss range. With the cold emission source, an energy resolution better than 0.6 eV could be achieved with this system. For the zirconium and yttrium $L_{2,3}$ edge spectra, to achieve maximum signal level at high energy loss as well as the appropriate total energy range, a large collector aperture and a small energy dispersion were used, reducing the energy resolution to ~3 eV. A higher energy dispersion was used to record the oxygen *K* edge, which led to an energy resolution of 0.9 eV.

For segregation analysis, EELS spectra were collected from bulk and grain-boundary areas for the Σ5 and near-Σ13 specimens. The initial energy-loss level was set to 2000 eV with an energy dispersion of 1 eV/channel, resulting in a spectrum ranging from ~2000 to 2380 eV. This energy range included the yttrium and zirconium L_2 and L_3 edges, which resulted from transitions from the $2p_{1/2}$ and $2p_{3/2}$ core levels into the unoccupied 4*d* states. Another possible range for segregation analysis containing the yttrium and zirconium $M_{4,5}$ and $M_{2,3}$ edges was ~200 eV; however, the broad yttrium and zirconium *M* edges overlapped, making quantitative analysis difficult. Because the oxygen *K*-edge fine structure is very sensitive to local coordination changes,[27,28] we also collected oxygen *K*-edge spectra from the grain interiors and grain boundaries. Spectra were collected while scanning an area 1 nm × 1.5 nm. To collect grain-boundary spectra, the scan area was precisely centered over the grain boundary, which could be simultaneously viewed in the dark-field image. Because of the long collection time (>30 s) required for each spectra, the image mode was essential for monitoring and correcting the specimen drift. EELS profiles were obtained by stepping the same scan area perpendicularly across the grain boundary. To remove multiple scattering effects, a low-loss spectrum was collected for each core-loss spectrum.

All spectra analyses were performed using EL/P™ software (Gatan, Pleasanton, CA). Spectra were corrected for channel-to-channel gain variations. Then, for each core-loss spectrum, the pre-edge background was subtracted and multiple scattering removed by a Fourier ratio deconvolution of its corresponding low-loss spectrum.[29] A further pre-edge background subtraction was needed for the zirconium $L_{2,3}$ edges, which was performed by assuming a constant yttrium L_2 edge continuum and subtracting its contribution to the zirconium $L_{2,3}$ edge. Finally, the partial energy-loss intensities for the yttrium and zirconium L_3 edges, I_Y and I_{Zr}, were obtained by integrating from the respective L_3 edge onset over a 50 eV energy window. The Y:Zr concentration ratio (r) was then obtained by normalizing the intensities by the theoretical partial cross sections (σ): $r = (I_Y/I_{Zr})(\sigma_{Zr}/\sigma_Y)$.

III. Results and Analysis

(1) Σ5 (310) Grain-Boundary Structure

The selected-area electron diffraction pattern of the 36.8° bicrystal is shown in Fig. 1(a), and it illustrates the crystallographic orientation relationship between the two halves of the YSZ bicrystal. This orientation relationship leads to a Σ5 coincident site

lattice that has a periodicity of 0.8 nm along [130] and 0.51 nm along the [001] tilt axis. A small misorientation of 0.6° between the two bicrystal halves was measured by convergent-beam electron diffraction.

A high-resolution *Z*-contrast STEM image taken from the grain boundary along the [001] projection is presented in Fig. 2, where the fast scan direction runs from left to right. The peaks of intensity in the image correspond to zirconium columns, or the cation sublattice. Because the image corresponds only to the projected structure, it is important to appreciate the cubic-ZrO_2 crystal structure (fluorite structure) in three dimensions. Figure 3 shows a ZrO_2 unit cell in which the zirconium atoms are distinguished by their position along [001], the beam direction. The zirconium atoms denoted by the filled circles are one-half unit cell below the zirconium atoms shown as open circles. Adjacent columns in the *Z*-contrast images, therefore, contain zirconium atoms displaced with respect to each other by 0.25 nm along the beam direction. The actual closest cation–cation distance is 0.36 nm. The oxygen columns, located between the zirconium columns, although within the resolution limit, are not detectable in the images because of the large tail on the zirconium scattering profile.

Although the lattice on either side of the boundary in Fig. 2 is easily resolved, the signal in the boundary region is lower because of strain-induced dechanneling, and individual columns are difficult to discern. To improve the signal-to-noise ratio in the boundary region, the image has been reconstructed by maximum entropy analysis as described above. The resulting object function, rotated so that the boundary runs horizontally, is presented in Fig. 4. With improved signal-to-noise ratio, columns in the boundary region are easily identifiable. The boundary region is composed of an array of similar structural units; the origin of each is identified by a white circle. Each structural unit has a similar shape; however, they are not identical because of the inherent resolution limit of the imaging technique and statistical structural differences. The average of the four grain-boundary units having the highest correlation is shown in Fig. 5. The signal-to-noise ratio is greatly enhanced in the averaged image, and, therefore, it is used for the model development. The correlation of the various units along the grain boundary in Fig. 4 with the average structure are, from left to right, 0.64, 0.79, 0.71, 0.86, 0.85, 0.82, and 0.85. To the right of the seventh unit in Fig. 4 is a portion of the grain boundary that has poor correlation with the average structural unit, indicating a defect structure. The statistical variations in the structure of each grain-boundary unit (average cross correlation = 0.79) are larger but on the order of that observed in the bulk structure (average cross correlation = 0.84).

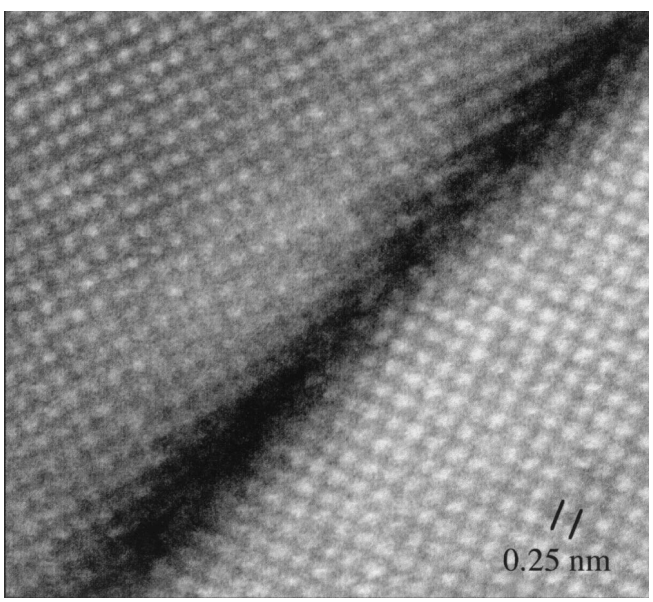

Fig. 2. *Z*-contrast STEM image of Σ5 YSZ grain boundary projected along the [001] tilt axis. White dots correspond to zirconium columns.

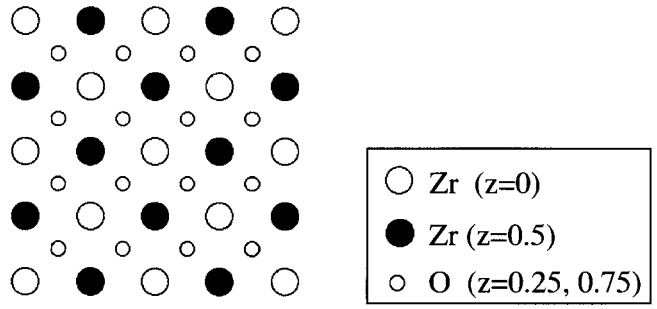

Fig. 3. Cubic-ZrO_2 crystal structure projected along the [001] tilt axis showing that adjacent zirconium columns are displaced by one-half of a unit cell along the direction of projection.

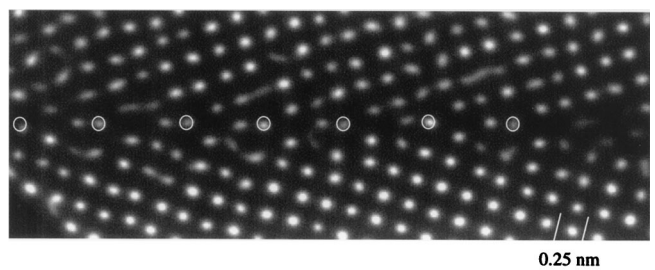

Fig. 4. Image of Σ5 YSZ grain boundary from Fig. 2 after maximum entropy processing. White circles identify the origin of each structural unit.

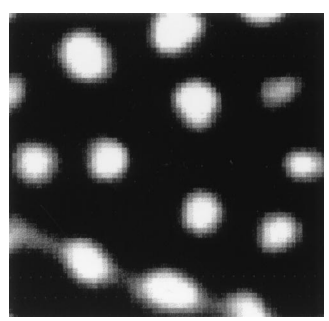

Fig. 5. Average Σ5 (310) YSZ grain-boundary structural unit.

Intensity fluctuations within the average core structure are observed in Fig. 5, but these cannot be interpreted as actual structural changes, because the fluctuations are as large as that measured in the bulk lattice. The smearing of intensities between zirconium columns in the lower bicrystal originates from the measured slight mistilt (0.6°) of the crystal.

(2) Near-Σ13 (510) Grain-Boundary Structure

The tilt angle of the near-Σ13 (510) bicrystal has been confirmed to be 24° about [001] by electron diffraction, as shown in Fig. 1(b). The perfect Σ13 (510) orientation corresponds to 22.6° tilt; therefore, the two boundaries should have similar local structures, but defects should be present in the 24° tilt to accommodate the mistilt. The repeat period of the Σ13 (510) is 0.25 nm along the [001] tilt axis and 1.23 nm along [510]; therefore, it has less translational symmetry than the Σ5 boundary. Therefore, fewer structural units in images taken at the same magnification are observed.

A *Z*-contrast image of the near-Σ13 YSZ grain boundary projected along the [001] zone axis is shown in Fig. 6, with the maximum entropy reconstruction in Fig. 6(b). Within the field of view, the boundary is composed of a periodic array of a basic structural unit, one of which is indicated by the open circles on Fig. 6(b). The average grain-boundary structure, averaged over

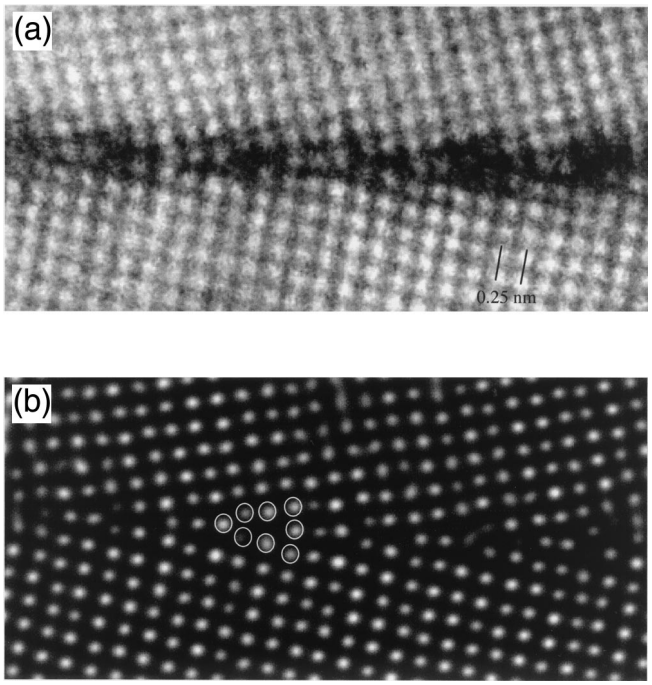

Fig. 6. (a) *Z*-contrast image of near-Σ13 symmetric tilt YSZ grain boundary and (b) after maximum entropy processing. White circles outline one of the periodic units.

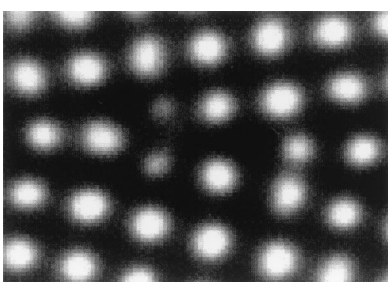

Fig. 7. Average near-Σ13 YSZ grain-boundary structural unit.

four units with the highest correlation, is shown in Fig. 7. The cross correlations between the various structural units in Fig. 6 (left to right) and the average structure have been calculated, yielding values of 0.93, 0.86, 0.90, and 0.70. Again, at the far right of the image, the last unit has poor correlation with the average, indicating a defect structure.

In the averaged near-Σ13, image fluctuations in the column intensities are also observed. These fluctuations, in particular the decreased intensity in two of the columns, are much greater than that measured in the bulk (50% in the grain boundary versus 15% in bulk). Because the decreased intensity in these two columns is much greater than the fluctuations in the bulk, we can interpret them as real structural changes. A decrease in the projected potential at these sites relative to the other cation columns would lead to such an intensity decrease.

(3) Electron Energy-Loss Spectroscopy

Both grain boundaries have been analyzed by energy-dispersive X-ray spectroscopy and low-dispersion EELS to inspect for the presence of impurity elements at the boundaries. Particular attention has been paid to the silicon *K* edge, because cosegregation of solute atoms with silicon has been demonstrated in CaO-stabilized ZrO_2, even when a discreet glassy phase is not formed at the grain boundaries.[14] No impurity elements, however, have been detected by either spectroscopy technique within their sensitivity limits.

Figure 8 shows the yttrium and zirconium $L_{2,3}$ edges from the bulk and grain boundary of the Σ5 (Fig. 8(a)) and near-Σ13 (Fig. 8(b)) tilt boundaries. The partial scattering cross sections for yttrium and zirconium L_3 edges used to convert the integrated intensities to concentrations have been computed using the Hartree–Slater approximation. Assuming that yttrium substitutes for zirconium, the actual yttrium density in units of atoms/(unit volume) can be computed knowing that the cation density is 32 atom/nm^3; these values are shown in Table I.

More thorough distribution profiles were obtained across the Σ5 grain boundary with spatially resolved EELS. Spectra were collected across the grain boundary in steps of 1 nm. The yttrium concentrations were obtained for each position and plotted as a function of the distance from the grain boundary (see Fig. 9). Yttrium segregation was highly localized at the grain boundary. In fact, there was no increase until as close as 2 nm, and the most significant increase occurred at the final 1 nm layer. This was the spatial limit of our measurement. Because there were only two unit cells within the scanned area, it was evident that most segregation occurred within the grain boundary core. To quantify the degree of solute segregation, we computed the Gibbsian interfacial excess (G),[30] as listed in Table I:

$$\Gamma = \int_{-w/2}^{w/2} (C^{gb}(x) - C^{bulk}) N \, dx$$

where $C^{gb}(x)$ is the measured solute concentration as a function of distance from the interface, C^{bulk} the average bulk concentration, and N the cation site density. The total interfacial excess is obtained by integrating over the boundary width w in which the concentration is not equal to the bulk concentration. Table I shows that Y^{3+} segregation at a level of 4.9 atoms/cm^2 is detectable at the Σ5 boundary, whereas no significant segregation is detected at the near-Σ13 boundary.

Figure 10 shows the oxygen *K*-edge spectra taken from the bulk ZrO_2 and the Σ5 grain boundary. The main fine structure features are the same in both spectra although the fine-structure intensities are suppressed in the grain-boundary spectrum. For comparison,

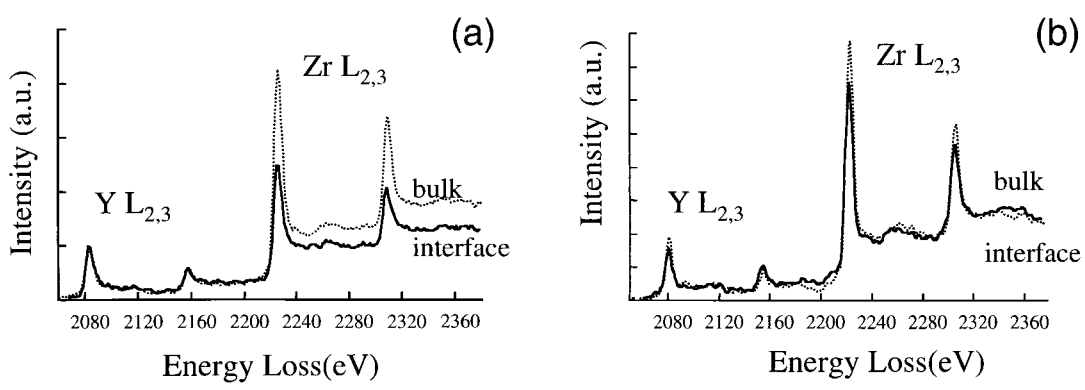

Fig. 8. Bulk and interface zirconium and yttrium $L_{2,3}$ EELS spectra from the (a) Σ5 and (b) near-Σ13 YSZ tilt grain boundaries.

Table I. Yttrium:Zirconium Concentration and Gibbsian Interfacial Excess

	$r_{Y:Zr}$	Y (at.%)	Y (atom/nm^3)	Γ ($\times 10^{14}$ atom/cm^2)
YSZ near-Σ13° (bulk)	0.179 ± 0.002	15.2 ± 2.0	4.8 ± 0.6	0.2 ± 1.4
YSZ near-Σ13 (interface)	0.182 ± 0.003	15.4 ± 2.8	4.9 ± 0.8	
YSZ Σ5 (bulk)	0.161 ± 0.002	13.9 ± 1.9	4.4 ± 0.6	4.9 ± 1.2
YSZ Σ5 (interface)	0.291 ± 0.002	22.6 ± 1.8	7.2 ± 0.6	

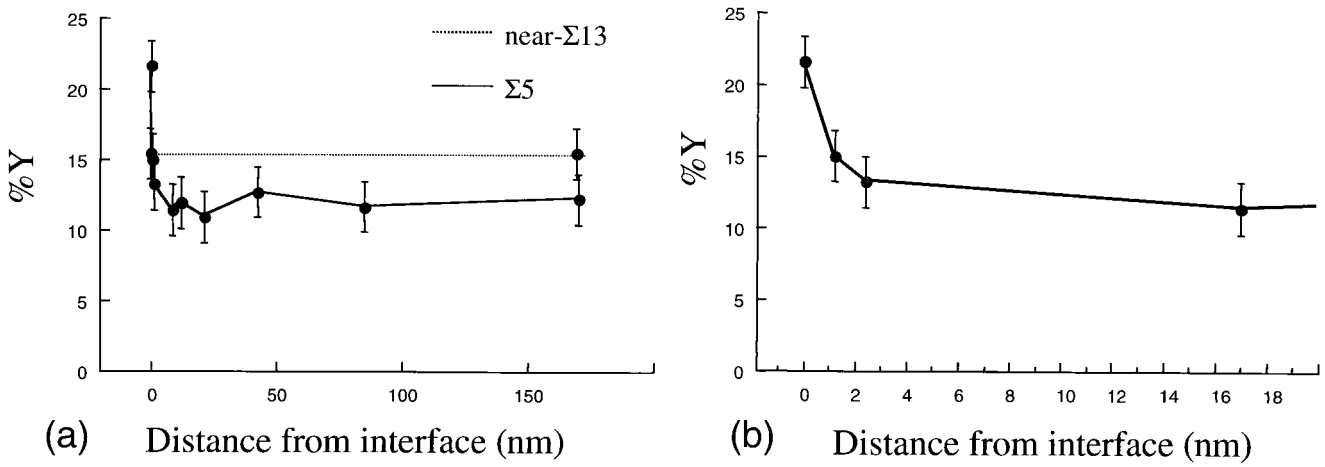

Fig. 9. (a) Yttrium concentration profile for the Σ5 and near-Σ13 grain boundaries. (b) Enlargement of (a) showing that the segregation to the Σ5 boundary is within 1 nm of the grain-boundary plane.

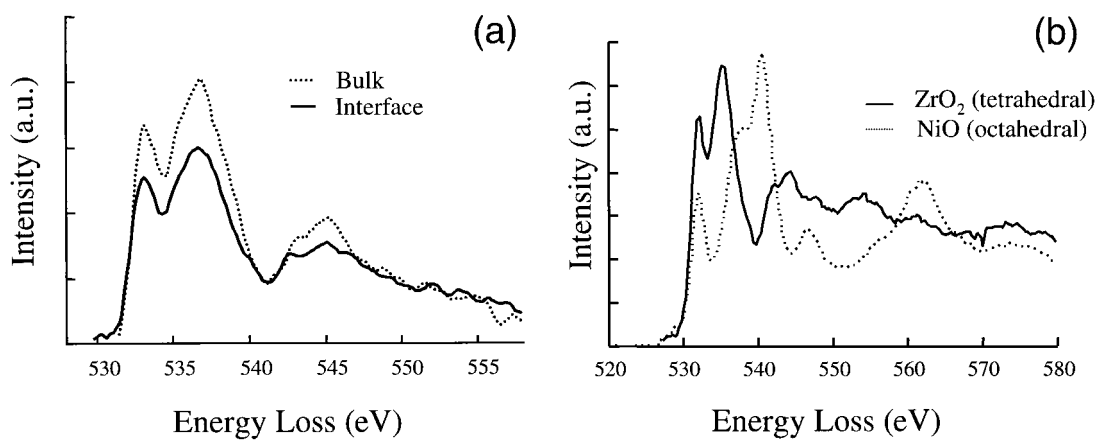

Fig. 10. (a) Oxygen *K*-edge EELS spectra from bulk and grain-boundary regions of the Σ5 YSZ bicrystal showing similar fine structures. (b) Spectra from ZrO_2 and NiO showing the pronounced effect that local coordination has on the oxygen *K*-edge fine structure.

Fig. 10(b) shows the dramatic changes in fine structure when the oxygen coordination changes from tetrahedral, as in ZrO_2, to octahedral, as in NiO. The fact that the predominant features in the oxygen *K*-edge fine structure are maintained at the grain boundary indicates that, on average, the oxygen ions are in a similar environment as the bulk oxygen. Major changes in local coordination would have led to a dramatic change in the fine structure.

IV. Discussion

(1) Σ5 (310) Grain Boundary

The intensities in Fig. 5 provide coordinates for the projected cation columns in the core of the Σ5 (310)/[001] grain boundary. Consistent with this experimental data, a model of the predominant Σ5 structural unit is presented in Fig. 11(b) next to an unrelaxed coincident site lattice (CSL) model in Fig. 11(a). Because EELS indicates that the oxygen ions are in tetrahedral-like environments, their positions have been chosen such that the oxygen ions maintain similar environments to that of the bulk. There are several other salient features of the model. The grain-boundary structural unit has near mirror symmetry, which leads to a continuity of the (200) planes across the grain-boundary plane. We conclude only that the boundary has *near* mirror symmetry, because rigid body translations (RBTs) are inherently difficult to quantify accurately from any type of high-resolution image. In phase-contrast imaging, image aberrations, such as twofold or threefold astigmatism or crystal tilt can provide substantial errors in RBT measurements unless taken specifically into account in image simulations.[31,32] In serially acquired high-resolution images, such as the *Z*-contrast images, errors can be introduced by mechanical or scan instabilities or drift. Within the experimental error, however, no in-plane rigid-body translations are observed, and the correlation coefficient between the structural unit and its mirror image is 0.86. Although the orthogonal component of the in-plane RBT along the [001] would not be apparent in the projected images, the model gives no overwhelming reason to suggest that such an offset would

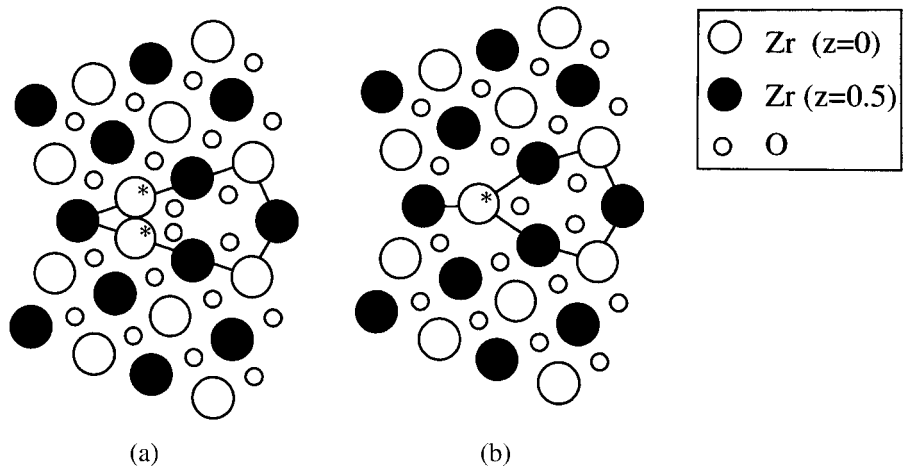

Fig. 11. (a) CSL model of Σ5 (310) YSZ grain boundary and (b) experimentally based model. See text for significance of asterisked columns.

be electrostatically favorable. The model, therefore, maintains the holosymmetric bicrystal symmetry of 2*mm*. Out-of-plane rigid-body translations, normal to the grain-boundary plane, also are not observed within experimental accuracy. A theoretical study of RBTs, which can determine these parameters well beyond the accuracy of the experimental data, are certainly warranted, because RBTs are known to be a common relaxation mechanism for grain boundaries.[33,34]

The most prominent feature of the Σ5 (310) grain-boundary structure is the local atomic relaxations within the grain-boundary core. We find that the two zirconium columns identified with asterisks in the unrelaxed CSL model of Fig. 11(a) are replaced with one single zirconium column located at the boundary plane (this column is identified with an asterisk in Fig. 11(b)). In the unrelaxed CSL model, adjacent zirconium atoms in the noted columns have a separation of only 0.16 nm, whereas the closest zirconium–zirconium spacing in the bulk is 0.36 nm. This cation crowding is apparently avoided by removing one zirconium column and moving the remaining column to an intermediate position. To maintain stoichiometry, a corresponding oxygen column must be removed, which also reduces the anion crowding. We have maintained stoichiometry in the model for simplicity. However, YSZ grain boundaries are believed to be positively charged, which indicates the presence of nonstoichiometric defects.[12,35]

This Σ5 (310) YSZ structural unit is remarkably similar to that of the model proposed by Kingery[36] for NaCl-type ceramics, which is shown in Fig. 12(a). In NaCl-type crystals, the projected columns along the [001] direction contain cations and anions, and adjacent columns are displaced by one-half of a unit cell along the beam direction. Experimentally derived structures for NiO Σ5 (310) grain boundaries by Merkle and Smith[9] are not consistent with the Kingery model; rather, they find the two core structures shown in Figs. 12(b) and (c). One of the boundary structures (Fig. 12(b)) has zero in-plane RBT, as predicted by Kingery, while the second structure (Fig. 12(c)) does not. The multiple structures result from step defects at the interface that introduce local in-plane rigid-body translations. Presumably, multiple boundary structures can exist in ZrO_2 as well; however, no stepped regions are encountered in the Σ5 (310) ZrO_2 specimens. The primary difference between the Kingery model and the Merkle "b" model of NiO is the combination of closely spaced adjacent columns in the boundary. Kingery has replaced the two columns with one located midway between the two, as is observed in our ZrO_2 grain boundary. Merkle's data, however, suggests that the columns remain intact and separated in NiO and that perhaps Shottkey defects are present in the boundary to reduce the crowding.

If we compare our ZrO_2 grain-boundary model to the two NiO models that maintain mirror symmetry (i.e., the Kingery model and Merkle "b" model), the differences between the structures can be understood in crystal-chemistry terms. In one sense, we might expect the NaCl-type and fluorite-type structures to have similar grain-boundary structures, because both are relatively simple binary oxide crystals. But, the anion sublattices are significantly different between the two crystal structures, simple cubic in ZrO_2 and face-centered cubic (fcc) in NaCl. From a purely electrostatic point of view, cation crowding in the grain-boundary core would be relatively unstable for ZrO_2. If we assume fully occupied columns in the unrelaxed CSL models, the nickel atoms in question are undercoordinated by one oxygen atom, whereas the zirconium atoms would be undercoordinated by two oxygen atoms. Moreover, the ionic repulsion between Zr^{4+} ions is much greater than between Ni^{2+} ions. Therefore, the electrostatic energy is higher in the unrelaxed fluorite boundary. In both cases,

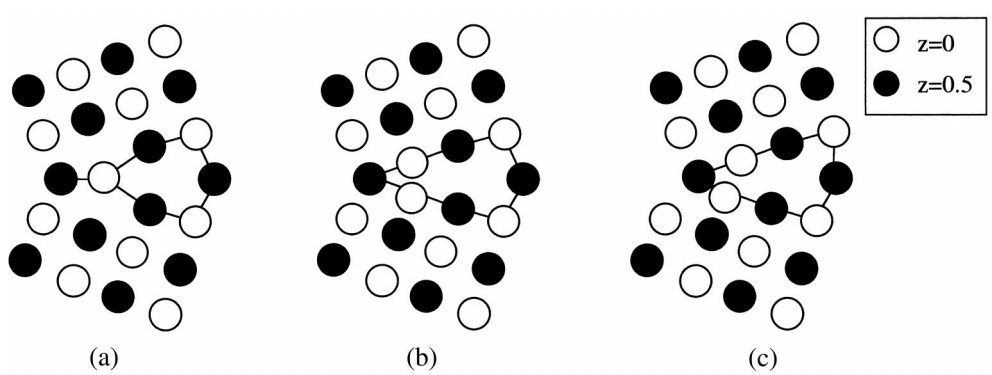

Fig. 12. Models of the NiO Σ5 (310) grain boundary: (a) proposed by Kingery,[36] (b) model "b" found by Merkel,[9] and (c) another asymmetric unit found by Merkle.[9] Kingery model is very similar to the unit found for ZrO_2.

Shottkey defects can reduce the free volume at the boundary to avoid ion crowding, but it appears that the boundary core shown in Fig. 11(b) is energetically favorable for the fluorite-type crystals.

(2) Near-Σ13 (510) Grain Boundary

The unrelaxed CSL model of the Σ13 (510) YSZ grain boundary is shown in Fig. 13(a) and compared with the model derived from the *Z*-contrast images in Fig. 13(b). As in the Σ5 boundary, within experimental accuracy, no rigid-body translations are evident, leading to a continuity of the (200) planes across the boundary. Therefore, the grain-boundary structural unit maintains 2*mm* symmetry.

The Σ13 grain-boundary core is completely different from and extended in comparison to the Σ5 grain-boundary core. The relaxation mechanisms also are different from in the Σ5 boundary. In the Σ13 CSL model (Fig. 13(a)), two pairs of columns are unrealistically close in the boundary core (>40% closer than the bulk zirconium–zirconium spacing). One has a spacing of 0.11 nm and the other 0.20 nm. As discussed above, this arrangement would be electrostatically unfavorable because of the large ionic repulsion. The pair of columns with the more severe, 0.11 nm, crowding is observed in the experimental data to be replaced by a shared column, similar to that found in the Σ5 boundary core. The columns separated by 0.20 nm, however, remain intact as two separate columns. In the bulk, the nearest zirconium–zirconium spacing is 0.36 nm; therefore, the close proximity of the zirconium ions in the grain boundary does not seem plausible. We do observe, however, that the intensities of these two columns in Fig. 7 are ~50% lower than that of the other zirconium columns. One cause of the decreased intensity could be a lowering of the projected potential resulting from cation vacancies in those columns. Partial occupancy would allow the zirconium atoms in the two adjacent columns to stagger along the beam direction and, thus, avoid close cation–cation positions. Similar observations have been made in other grain-boundary studies, including those of $SrTiO_3$[11,37] and $YBa_2Cu_3O_{7-x}$.[38] Again, the oxygen positions in the grain-boundary model have been chosen such that they are most similar to the positions in bulk ZrO_2.

(3) Comparison of the Σ5 and Near-Σ13 Symmetric Tilt YSZ Grain Boundaries

The Σ5 and near-Σ13 boundaries are observed to have highly symmetrical core structures that maintain near mirror symmetry across the boundary plane. In the unrelaxed CSL models, several cation columns are unrealistically close, leading to increased atom density and ionic repulsion. The *Z*-contrast images indicate two alternative structures that prevent this cation crowding. The first, as observed in both grain-boundary cores, is that the total atom density is reduced in the area, and one column, instead of two, is located symmetrically at the boundary plane. The second possible structure is one in which the two closely spaced columns contain a high fraction of cation vacancies to avoid close cation positions. The data suggest that there may be a critical separation (between 0.16 and 0.20 nm) below which adjacent half-filled columns are replaced by a single intermediate column, but no definite conclusions can be made at this time.

The fact that two completely different grain-boundary structures are observed for the two boundaries has implications for the grain-boundary structural unit model.[39,40] This model suggests that special high-symmetry grain boundaries have specific, delimiting grain-boundary structural units. Other grain boundaries, which fall in misorientation between the delimiting boundaries, are composed of combinations of the delimiting boundary units. For example, Wang *et al.*,[4] have calculated the structure of a range of [001] tilt grain boundaries in copper. They have found the 22.6° Σ13 boundary to be composed of a combination of structural units from the delimiting 0° misorientation, or perfect crystal, and the 36.8° Σ5 boundary (i.e., Σ5 cores separated by coincident planes). In the present study, we find two completely different grain-boundary cores for the Σ5 and near-Σ13 boundaries. Because ionically bonded materials are intrinsically more sensitive to small atomic displacements than metals (i.e., higher bond stiffness), there should be many delimiting boundaries for ionic materials.

The different core structures also exhibit different interfacial chemistries, in particular, the solute segregation observed at the Σ5 boundary but not the near-Σ13 boundary. Excess yttrium at free surfaces and interfaces has been observed in many studies of YSZ[17,41] although the driving force for the segregation has been debated. Several studies have indicated that the solute segregation is space-charge induced.[12,35] Aoki *et al.*,[14] however, have shown that calcium segregation in CaO-stabilized ZrO_2 is grain-size dependent and strongly correlated with silicon segregation. Grain-size-dependent segregation behavior observed in YSZ also suggests cosegregation of yttrium and silicon.[41] Aoki *et al.* have observed in fine-grained specimens, which exhibit virtually no silicon segregation, that calcium segregates to ~50% of the grain boundaries at an average level of 1.8 atoms/cm^2. It is possible that multiple driving forces for solute segregation in ZrO_2 exist, and when cosegregation with silicon is not operative, other driving forces (e.g., electrostatic or elastic) are significant. In the present study, silicon is not detected at either grain boundary; therefore, cosegregation with silicon does not appear to be a driving force for solute segregation. Although no measurable solute segregation is present at the near-Σ13 boundary, an excess of $(4.9 \pm 1.2) \times 10^{14}$ atoms/cm^2 is detected at the Σ5 boundary. The origins of this anisotropic segregation behavior are not clear at this time.

Grain-boundary segregation of impurities can induce structural changes at grain boundaries. For example, the Σ5 (310) grain boundary in MgO, although expected to have the same structure as NiO (Fig. 12(b)), maintains a unique core structure, attributed to calcium segregation to the grain-boundary core.[42] In this study, however, the Y^{3+} solute concentrations are similar in both bicrystals. Because the chemistry and local structure are inextricably coupled in a multidimensional phase space, it is not possible to conclude that the solute segregation causes different core structures in the Σ5 and near-Σ13 boundaries. We can, however, conclude that the two grain boundaries do exhibit significantly different core structures, in terms of chemistry and local atom positions and, therefore, should exhibit distinct physical properties.

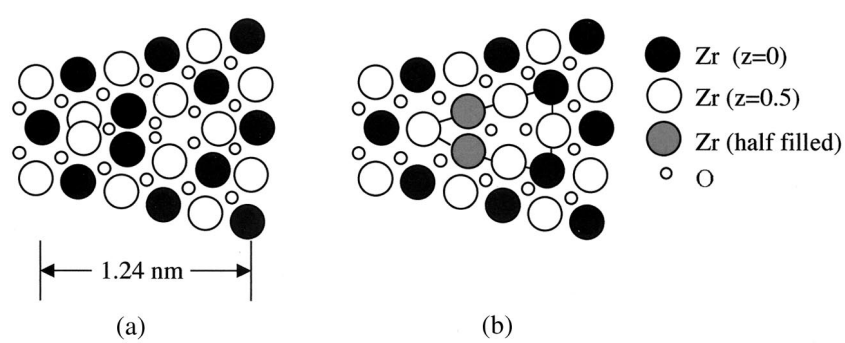

Fig. 13. (a) CSL model of Σ13 (510) YSZ grain boundary and (b) experimentally based model.

V. Conclusions

Atomic models of the Σ5 (310)/[001] and near-Σ13 (510)/[001] symmetric tilt YSZ grain boundaries have been developed from *Z*-contrast STEM images and complementary EELS. Both grain boundaries have relatively simple, high-symmetry structural units with no observable symmetry-breaking rigid-body translations within experimental accuracy. The oxygen positions in the models are chosen such that they are in distorted tetrahedral sites, as suggested by the EELS data. The two grain boundaries exhibit distinct boundary cores, with an extended core in the near-Σ13 boundary. Solute segregation to the grain boundaries also is significantly different. Although no segregation is present at the near-Σ13 boundary, an interfacial excess of 4.9×10^{14} atoms/cm^2 has been measured at the Σ5 boundary with no evidence of cosegregation with silicon. The fact that two distinct cores are observed in boundaries varying by only a 12.6° mistilt highlights the need for care when applying the structural unit model to ionic grain boundaries, especially when solute atoms are involved.

Based on the experimentally derived grain-boundary structures, we are currently pursuing complementary theoretical density functional calculations. Through the atomistic calculations, we hope to refine the atomic positions and translation states beyond the experimental accuracy and understand the origins of the different grain boundary structures.

References

[1]R. W. Balluffi, A. Brokman, and A. H. King, "CSL/DSC Lattice Model for General Crystal–Crystal Boundaries and Their Line Defects," *Acta Metall.*, **30,** 1453–70 (1982).

[2]A. P. Sutton and R. W. Balluffi, "On Geometric Criteria for Low Interfacial Energy," *Acta Metall. Mater.*, **35,** 2177–201 (1987).

[3]R. C. Pond and D. S. Vlachavas, "Bicrystallography," *Proc. R. Soc. London A*, **386,** 95–143 (1983).

[4]G. J. Wang, A. P. Sutton, and V. Vitek, "A Computer Simulation Study of <001> and <111> Tilt Boundaries: The Multiplicity of Structures," *Acta Metall.*, **32,** 1093–104 (1984).

[5]G. H. Campbell, S. M. Foiles, P. Gumbsch, M. Rühle, and W. E. King, "Atomic Structure of the (310) Twin in Niobium: Experimental Determination and Comparison with Theoretical Predictions," *Phys. Rev. Lett.*, **70,** 449–52 (1993).

[6]G. H. Campbell, J. Belak, and J. A. Moriarty, "Atomic Structure of the Σ5 (310)/[001] Symmetric Tilt Grain Boundary in Molybdenum," *Acta Mater.*, **47,** 3977–85 (1999).

[7]R. W. Fonda and D. E. Luzzi, "High-Resolution Electron Microscopy of the Σ = 5 [001] (310) Grain Boundary in NiAl," *Philos. Mag. A*, **68,** 1151–64 (1993).

[8]R. W. Fonda, M. Yan, and D. E. Luzzi, "Atomic Structure of the Σ = 5 (310) [001] Grain Boundary in NiAl: A Combined Electron Microscopy and Theoretical Study," *Philos. Mag. Lett.*, **71,** 221–28 (1995).

[9]K. L. Merkle and D. J. Smith, "Atomic Structure of Symmetric Tilt Grain Boundaries in NiO," *Phys. Rev. Lett.*, **59,** 2887–90 (1987).

[10]V. Ravikumar and V. P. Dravid, "Atomic Structure of Undoped Sigma = 5 Symmetrical Tilt Grain-Boundary in Strontium Titanate," *Ultramicroscopy*, **52**, 557 (1993).

[11]M. M. McGibbon, N. D. Browning, M. F. Chisholm, A. J. McGibbon, V. Ravikumar, and V. P. Dravid, "Direct Determination of Grain Boundary Atomic Structure in $SrTiO_3$," *Science (Washington, DC)*, **261,** 102–104 (1994).

[12]X. Guo, "Physical Origin of the Intrinsic Grain-Boundary Resistivity of Stabilized-Zirconia: Role of the Space-Charge Layers," *Solid State Ionics*, **81,** 235–42 (1995).

[13]D. M. Owen and A. H. Chokshi, "The High-Temperature Mechanical Characteristics of Superplastic 3 mol% Yttria-Stabilized Zirconia," *Acta Mater.*, **46,** 667–79 (1998).

[14]M. Aoki, Y.-M. Chiang, I. Kosacki, L. J. Lee, H. Tuller, and Y. Liu, "Solute Segregation and Grain-Boundary Impedance in High-Purity Stabilized Zirconia," *J. Am. Ceram. Soc.*, **79,** 1169–80 (1996).

[15]M. J. Merkerk, B. J. Middelhuis, and A. J. Burggraaf, "Effect of Grain Boundaries on the Conductivity of High-Purity ZrO_2–Y_2O_3 Ceramics," *Solid State Ionics*, **6,** 159–70 (1982).

[16]K. L. Merkle, G.-R. Bai, Z. Li, C.-Y. Song, and L. J. Thompson, "High-Resolution Studies of Grain Boundary Structure in Yttria-Stabilized Cubic Zirconia Thin Films Grown by MOCVD," *Phys. Status Solidi*, **166,** 73–89 (1998).

[17]G. S. A. M. Theunissen, A. J. A. Winnubst, and A. J. Burggraaf, "Surface and Grain Boundary Analysis of Doped Zirconia Ceramics Studied by AES and XPS," *J. Mater. Sci.*, **27,** 5057–66 (1992).

[18]D. E. Jesson and S. J. Pennycook, "Incoherent Imaging of Thin Specimens Using Coherently Scattered Electrons," *Proc. R. Soc. London A*, **441,** 261–81 (1993).

[19]D. E. Jesson and S. J. Pennycook, "Incoherent Imaging of Crystals Using Thermally Scattered Electrons," *Proc. R. Soc. London A*, **449,** 273–93 (1995).

[20]P. D. Nellist, "Incoherent Imaging Using Dynamically Scattered Coherent Electrons," *Ultramicroscopy*, **78,** 111–24 (1999).

[21]S. F. Gull and G. J. Daniell, "Image Reconstruction from Incomplete and Noisy Data," *Nature (London)*, **272,** 686–90 (1978).

[22]S. F. Gull and J. Skilling, "Maximum Entropy Method in Image Processing," *IEE Proc.*, **131F**, 646–59 (1984).

[23]P. D. Nellist and S. J. Pennycook, "Accurate Structure Determination from Image Reconstruction in ADF STEM," *J. Micros.*, **190**, 159–70 (1998).

[24]A. J. McGibbon, S. J. Pennycook, and D. E. Jesson, "Crystal Structure Retrieval by Maximum Entropy Analysis of Atomic Resolution Incoherent Images," *J. Micros.*, **195,** 44–57 (1999).

[25]S. Paciornik, R. Kilaas, J. Turner, and U. Dahmen, "A Pattern Recognition Technique for the Analysis of Grain Boundary Structure by HREM," *Ultramicroscopy*, **62,** 15–27 (1996).

[26]D. McMullan, J. M. Rodenburg, Y. Murooka, and A. J. McGibbon, "Parallel EELS CCD Detector for a VG HB501 STEM," *Inst. Phys. Conf. Ser.*, **98,** 55–58 (1990).

[27]P. Rez, X. Weng, and H. Ma, "The Interpretation of Near Edge Structure," *Microsc. Microanal. Microstruct.*, **2,** 1–99 (1991).

[28]L. A. Grunes, R. D. Leapman, C. N. Wilker, and R. Hoffman, "Oxygen *K* Near-Edge Fine Structure: An Electron-Energy-Loss Investigation with Comparisons to New Theory for Selected 3*d* Transition-Metal Oxides," *Phys. Rev. B*, **25,** 7157–73 (1982).

[29]R. F. Egerton, *Electron Energy-Loss Spectroscopy in the Electron Microscope*, 2nd ed.; p. 264. Plenum Press, New York, 1996.

[30]J. A. S. Ikeda, Y.-M. Chang, A. J. Garratt-Reed, and J. B. V. Sande, "Space Charge Segregation at Grain Boundaries in Titanium Dioxide: II, Model Experiments," *J. Am. Ceram. Soc.*, **76,** 2447–59 (1993).

[31]K. L. Merkle, R. Csenscits, K. L. Rynes, J. P. Withrow, and P. A. Stadelmann, "The Effect of Three-Fold Astigmatism on Measurements of Grain Boundary Volume Expansion by High-Resolution Transmission Electron Microscopy," *J. Micros.*, **190,** 204–13 (1997).

[32]R. Schweinfest, F. Ernst, T. Wagner, and M. Rühle, "High-Precision Assessment of Interface Lattice Offset by Quantitative HREM," *J. Micros.*, **194,** 142–51 (1999).

[33]M. J. Weins, H. Gleiter, and B. Chalmers, "Computer Calculations of the Structure and Energy of High-Angle Grain Boundaries," *J. Appl. Phys.*, **42,** 2639–45 (1971).

[34]D. Wolf, "Structure–Energy Correlations for Grain Boundaries in FCC Metals—II. Boundaries on the (110) and (113) Planes," *Acta Metall. Mater.*, **37,** 2823–33 (1989).

[35]S.-L. Hwang and I-W. Chen, "Grain Size Control of Tetragonal Zirconia Polycrystals Using the Space Charge Concept," *J. Am. Ceram. Soc.*, **73,** 3269–77 (1990).

[36]W. D. Kingery, "Plausible Concepts Necessary and Sufficient for Interpretation of Ceramic Grain-Boundary Phenomena: I, Grain-Boundary Characteristics, Structure, and Electrostatic Potential," *J. Am. Ceram. Soc.*, **57,** 1–8 (1974).

[37]M. M. McGibbon, N. D. Browning, A. J. McGibbon, and S. J. Pennycook, "The Atomic Structure of Asymmetric [001] Tilt Boundaries in $SrTiO_3$," *Philos. Mag. A*, **73,** 625–41 (1996).

[38]N. D. Browning, P. D. Nellist, D. P. Norton, M. F. Chisholm, and S. J. Pennycook, "The Atomic Origins of Reduced Critical Currents at [001] Tilt Grain Boundaries in $YBa_2Cu_3O_{7-\delta}$ Thin Films," *Physica C*, **294**, 183–93 (1998).

[39]A. P. Sutton and V. Vitek, "On the Structure of Tilt Grain Boundaries in Cubic Metals I. Symmetrical Tilt Boundaries," *Philos. Trans. R. Soc. London*, **A309,** 1–36 (1983).

[40]A. P. Sutton and V. Vitek, "On the Structure of Tilt Grain Boundaries in Cubic Metals II. Asymmetrical Tilt Boundaries," *Philos. Trans. R. Soc. London*, **A309,** 37–54 (1983).

[41]M. M. R. Boutz, C. S. Chen, L. Winnubst, and A. J. Burggraaf, "Characterization of Grain Boundaries in Superplastically Deformed Y-TZP Ceramics," *J. Am. Ceram. Soc.*, **77,** 2632–40 (1994).

[42]Y. Yan, M. F. Chisholm, G. Duscher, and S. J. Pennycook, "Impurity-Induced Structural Transformation of a MgO Grain Boundary," *Phys. Rev. Lett.*, **81,** 3675–78 (1998). □